Research Article

Nano Research
2023, 16(7): 10100–10107

ISSN 1998-0124 CN 11-5974/O4
https://doi.org/10.1007/s12274-023-5709-8

Printable microlaser arrays with programmable modes for information encryption

Jun Ruan, Dan Guo (✉), Kun Ge, Zhiyang Xu, Fangyuan Liu, and Tianrui Zhai (✉)

College of Physics and Optoelectronics, Faculty of Science, Beijing University of Technology, Beijing 100124, China

Received: 12 February 2023 / **Revised:** 28 March 2023 / **Accepted:** 5 April 2023

ABSTRACT

Lasing emissions with multiple and tunable modes are promising in coding field as a novel cryptographic primitive. With the advantages of simple fabrication, full-color and high-quality-factor whispering gallery mode lasing inside a circular cross-section, polymer microfibers are attractive for photonic devices. However, polymer lasing microfibers for information encryption have never been reported. Herein, we propose a design of printable lasing microfiber encryption chip by *in-situ* tuning the effective refractive index of the microresonator arrays via a facile approach. Through inkjet printing high-refractive-index nanoparticles on the designated position of lasing microfiber arrays, the effective refractive index of the microcavities is regulated, and the ratio of wavenumber spacing between transverse electric and transverse magnetic mode to the free spectral range can be modulated, particularly with neglectable influence by the size factor. Thus, the programmable region selective encoding process can be conducted simply by a printing program within several minutes. Besides, the encoded microfiber arrays are encapsulated into polydimethylsiloxane to reduce the scattering loss and environmental interference, and a printable encryption chip is realized. This work is expected to provide a platform for the printable encrypted devices.

KEYWORDS

polymer microfiber, whispering gallery mode microcavity laser, polarization, mode spacing, optical encryption

1 Introduction

As information security plays an increasingly significant role in military, financial field and daily lives [1–3], confidential tags with high hiding and security are urgently required and have attracted tremendous interest. With merit of easy operation, multiplexing and efficient authentication, optical encryption has been widely applied in information security as a common encryption method [4–8]. So far, many methods have been developed to improve encryption security level, such as expanding the light-emissive range [9], using luminescence lifetime multiplexed encoding [10, 11], developing multi-stimuli responsive materials [12–14], utilizing surface enhanced Raman scattering (SERS) [15, 16], as well as employing lasing signals [17, 18]. In comparison with broad-band photoluminescence (PL), lasing emissions with narrow linewidth have the advantage of easily distinguishable readout [19, 20], and contain multiple information including linewidth, polarization, quality factor (Q), lasing modes, and threshold, etc.[21–27] Whispering gallery mode (WGM) lasers possess the superiorities of high quality, small mode volume and easy processing [28–31], and have surface modes that propagate azimuthally around resonators with rotational symmetry [32–34]. These modes are resonant in optical wavelength, and the spectral position of the resonances depends on radius and refractive index of the microresonator, as well as the external medium [35, 36]. Thus, WGM is always used to characterize the microcavity parameters and sense the environmental interference (such as temperature, strain, molecules and nanoparticles), mainly through detecting the frequency shifts [37, 38], linewidth broadening [39], polarization [40, 41] and multi-mode properties [42]. These properties can provide multiple coding information, and the past five years have witnessed the development of fabricating microlaser arrays with tunable lasing properties to form encryption devices, such as encoding the readout of mode frequency through regulating group refractive index of the microcavity [43], recording the threshold of perovskite microlasers in different shapes [44], and modulating the multiple emission states of responsive organic microlasers [45]. These microcavities arrays are precisely fabricated by electron beam lithography to ensure the size controllability. Polymer microfibers, with the advantages of simple fabrication, full-color, good mechanical flexibility and high Q, enabling WGM lasing oscillation inside a circular cross-section, have shown the applications in refractive index or mechanical sensors based on the shifting or splitting of resonance modes [46, 47]. However, polymer lasing microfibers for information encryption have never been reported.

Herein, we develop a facile strategy to fabricate lasing microfiber arrays with region selective encoding with programmable modes for information encryption. The lasing microfibers are assembled into arrays to provide the substrate for encoding. By *in-situ* tuning the effective refractive index of the microcavities through inkjet printing high-refractive-index titanium dioxide nanoparticles (TiO_2 NPs) on the designated position of the lasing microfiber arrays, the ratio of wavenumber spacing ($\Delta 1/\lambda$) between transverse electric (TE) and transverse magnetic (TM) modes with the same angular quantum number to

Address correspondence to Dan Guo, dguo@bjut.edu.cn; Tianrui Zhai, trzhai@bjut.edu.cn

free spectral range (FSR) can be modulated to achieve programmable region selective encoding, with neglective influence by the microresonator size factor. To reduce the scattering loss and environmental interference, the encoded lasing microfiber arrays are encapsulated in polydimethylsiloxane (PDMS), and the printable encryption chip with stable and programmable information storage capability is realized.

2 Experimental section

2.1 Preparation of microfibers

Polyvinyl alcohol (PVA, M_W = 198,000 g·mol^{-1}) was dissolved in deionized water with the concentration of 176 mg·mL^{-1}. Then sodium dodecyl sulfate (SDS) and laser dye were subsequently added into the solvated PVA. The concentration of SDS in deionized water was 50 mg·mL^{-1}. The concentrations of the laser dye of Rhodamine B (RhB) in deionized water was 6 mg·mL^{-1}. Finally, these were thoroughly mixed to form homogeneous solution by a magnetic stirrer at 60 °C for 6 h. The as-prepared solution was carefully loaded into a 2.5-mL syringe, and the squeezing flux was controlled by a micro-syringe pump. The viscous liquid fell from a syringe nozzle to form elongating liquid filament driven by equilibrating its gravity and viscosity. The formed liquid filament was gradually collected by the rotatory drum in succession. In this experiment, the rotating speed of the drum was 3 rpm, and the squeezing flux of solutions was controlled at 1 mL·h^{-1}. The translational velocity of the syringe was 3 mm·s^{-1}. The distance between the syringe tip and the drum collector was set at 10 cm for the formation of even filament. The experiment was operated in the ambient environment.

2.2 Inkjet printing

The ink was prepared by dispersing TiO_2 NPs with the diameter of 40 nm in ethanol with the concentration of 0.02 mg·mL^{-1}, and was printed onto the aligned microfiber arrays by a high-precision piezoelectric inkjet printer (Microfab JETLAB 4, Microfab Technologies Inc.). We chose the inkjet nozzle with the diameter of 60 μm to form the ink droplet that is able to cover the surface of a microfiber. The experiment was operated in the ambient environment.

2.3 Lasing characterization

A nanosecond laser at a wavelength of 532 nm (Q-switched second harmonics from a 1064 nm Nd:YAG pulsed laser, a repetition frequency of 10 Hz, and a pulse width of 1 ns) was coupled into a microscopy, which was connected with Princeton Instrument (PI) Spectrometer. For dyes of S420 and Uranin, a nanosecond laser at a wavelength of 343 nm (third harmonics from a 1030 nm Yb:YAG laser, a repetition frequency of 200 Hz, and a pulse width of 1 ns) was used. The emission spectra were collected by a spectrometer with 2400 g·mm^{-1}.

3 Results and discussion

The design principle of the lasing encryption chip is based on the sensitivity of WGM to effective refractive index, which will affect the effective optical path inside the microresonators. For WGM microfiber lasers in this work, both TE and TM resonance modes are sustained simultaneously, and the mode spacings between TE and TM polarizations, as well as the FSR, are affected by the effective refractive index of microresonators (supplementary notes in the Electronic Supplementary Material (ESM)). These WGM lasing characteristics can be manipulated by inkjet printing high-refractive index nanoparticles on the designate position of the microfibers. As a result, these aligned microfibers, serving as microlasers arrays with programmable mode information, can be used to encrypt the information. To realize the large information encryption capacity, we prepared and arranged the polymer microfibers that can be large-area processed as the unencrypted microlaser arrays, and regulated the mode spacing between TE and TM polarizations of lasing spectra through modulating refractive index of the microcavity at the designated site by inkjet printing TiO_2 NPs via a digital programmable printer. In order to eliminate the interruptions from the uneven size in the polymer microfibers to ensure the encryption stability, we elaborately extracted the ratio of $\Delta 1/\lambda$ to FSR as the coding element, to read out the covert cryptogram of encrypted information from the lasing spectra of the printed microfibers.

The scheme of fabrication for the lasing encryption chip based on WGM lasing microfibers is illustrated in Fig. 1(a). Typical laser dye RhB was employed as the gain material, with PL emission in red wavebands (Fig. S1 in the ESM). The solution used for microfiber fabrication was prepared by mixing PVA, SDS and RhB in deionized water. Addition of SDS is vital to control the solution viscosity for stabilize the microfibers formation, and the polymer microfibers were obtained by a gravity assisted rotatory drawing (GARD) method [48]. The formed microfibers show high-quality-factor whispering gallery mode lasing inside a circular cross-section (Fig. S2 in the ESM), and can be arranged into suspended arrays on a support frame. Then, the surface of the suspended microfibers was deposited with TiO_2 NPs at the designate site via inkjet printing technique to achieve encoding. Subsequently, the printed suspended microfiber arrays were carefully placed into the uncured PDMS that was coated on a glass substrate. After curing, PDMS film encapsulating the microlaser arrays was peeled off the glass substrate to form a free-standing membrane. The encapsulation of PDMS elastomer can not only reduce the interface scattering loss, but also provide good mechanical flexibility, optically transparency and chemical inert to avoid the environmental interference [49].

The TiO_2 NPs with diameter of about 40 nm (Fig. S3 in the ESM) were dispersed in ethanol to prepare the ink, because polymer matrix of PVA cannot be dissolved in ethanol. After the evaporation of solvent, TiO_2 NPs depositing on the surface of the microfiber can serve as a high-refractive-index cladding, thus influencing the effective refractive index of the microcavity (n_{cav}). Besides, the distribution density of TiO_2 can be tuned by the times of inkjet printing, which can be used to tune n_{cav}. The lasing emission properties from the printed-microfibers were investigated by a microscopic PL spectra measurement combined with linear polarizers and a half wave plate (HWP) (Fig. 1(b)). The polarization behavior of the microfiber laser was made out by a linear polarizer. Besides, the polarization direction of the pumping source in the excitation optical path was adjusted by rotating the HWP to investigate the dependence of lasing polarization properties on the angle between polarization direction of the pumping source and axial direction of the microfiber. The lasing emission spectra show that the wavelength spacing between TE and TM polarizations ($\Delta\lambda$) of the printed microfiber is larger than that of the pristine one (Fig. 1(c)). The increase of the mode spacing is attributed to the increase of n_{cav}, which is caused by the coating of TiO_2 NPs with high refractive index (supplementary notes in the ESM). On this basis, the mode spacing of TE and TM lasing polarizations can be regulated controllably, which can be applied in information encryption or encoding.

Owing to the natural circular cross section and smooth surface, the microfibers can serve as high-quality WGM resonators for laser oscillations (Fig. S4 in the ESM), even after the surface is covered with TiO_2 NPs. Moreover, the encapsulation of PDMS

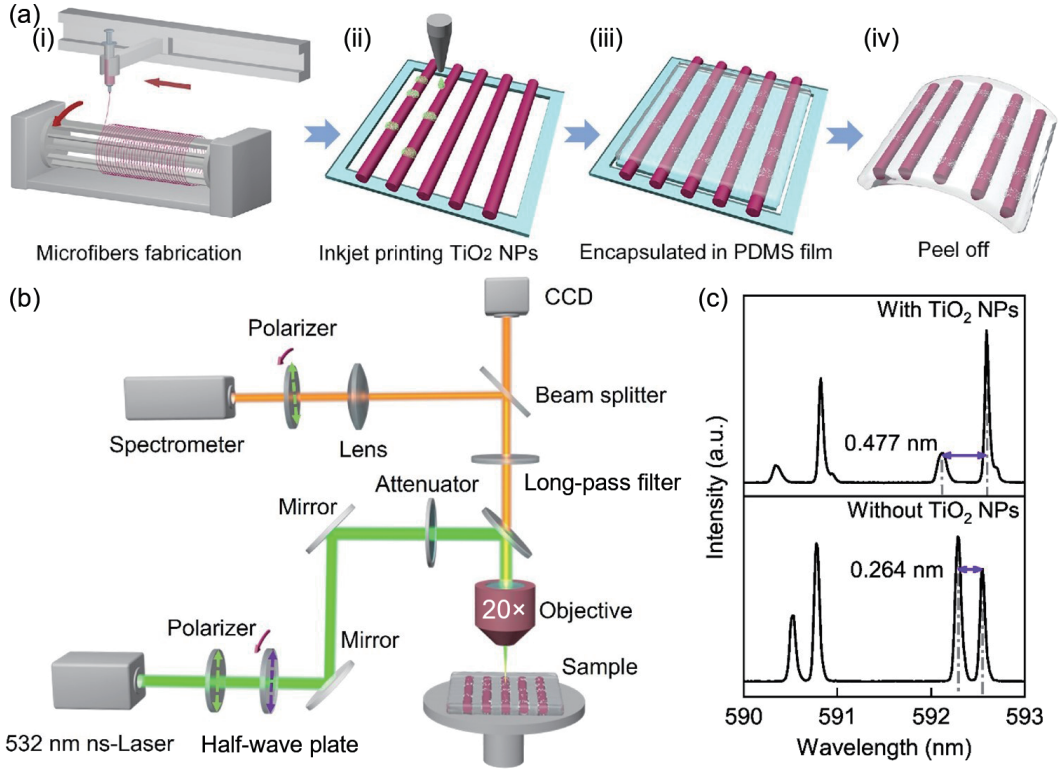

Figure 1 (a) Scheme illustration of the fabrication for the free-standing encryption chip based on WGM lasing microfibers by GARD method and inkjet printing process. (b) Schematic setup for microscopic PL spectra measurement for free-standing encryption chip. (c) Lasing spectra of microfibers with and without printing TiO_2 NPs.

can reduce interface scattering caused by the roughness of the microfiber surface and TiO_2 NPs (Fig. S5 in the ESM). The PL spectra evolution of the printed microfiber with the diameter of 43 μm, under the gradually increased pump fluences as shown in Fig. 2(a). At low pump fluence, the PL spectra are dominated by broad spontaneous emission. When the pump fluence exceeds 71.4 μJ·cm^{-2}, the emission spectra develop into a set of sharp peaks, indicating the formation of stimulated emission. The lasing spectra of microfiber show a series of two distinct separated lasing envelopes, which may represent TE and TM modes [50]. The wavelength spacing between these two adjacent modes is about 0.542 nm, which is larger than the pristine one (Fig. S6 in the ESM). Moreover, the full width at half maximum (FWHM) is measured to be 0.041 and 0.042 nm, corresponding to a high Q of 14,100 and 14,400 according to the relation $Q = \lambda_0/\lambda_{FWHM}$, respectively (Fig. S7 in the ESM). To verify the characteristics of TE and TM modes, the polarization properties of the printed WGM microfiber laser were investigated. Using a linear polarizer in the measurement optical path, the obtained lasing spectra of WGM in TM, TM&TE mixed and TE validates that polarized TE and TM modes can be simultaneously excited in WGM microfiber laser (Fig. 2(b) and Fig. S8 in the ESM). The polar plot (Fig. 2(c)) deduced from Fig. 2(b) clearly shows the orthogonal character of these two sets of modes. These results further confirm the two sets of peaks are TE and TM polarization modes, respectively. Besides, by tuning relative angle between polarization direction of the pump laser and axial direction of the microfiber, both TE and TM lasing modes can be observed simultaneously, with the fixed $\Delta\lambda$ of 0.386 nm, showing the stability of two sets of lasing modes (Fig. 2(e)). Note that the result is different from the previous work with dye molecules dispersed in the liquid [51], it can be attributed that the dye molecules embedded in the solid polymer matrix will not be influenced by the polarization of pump laser.

The plots of PL intensity and FWHM versus pump fluence exhibit a clear knee behavior characteristic, with a threshold about 71.4 and 89.5 μJ·cm^{-2} for TE and TM polarization, respectively (Fig. 2(d)). The lasing threshold was also investigated before and after inkjet printing process (Fig. S9 in the ESM). The result shows that the threshold does not increase significantly compared to the unprinted microfiber. Meanwhile, lasing threshold of the printed microfiber without PDMS encapsulation is 67.7 μJ·cm^{-2} for TM mode, which is lower than that with PDMS encapsulation (Fig. S10 in the ESM). It can be attributed to the higher refractive index of PDMS than air. Besides, this strategy of mode spacing modulation is also applicable to different laser dyes (Fig. S11 in the ESM) and different polymer matrix (Fig. S12 in the ESM), further confirming the feasibility of this strategy.

We built physical models of the composite microresonators by integrating the inner active core fiber with a composite cladding layer of PDMS mixed with different density of TiO_2 NPs (Fig. 3(a)), and simulated the mode-field intensity distribution of the composite micresonators (Fig. 3(b)). The effective refractive index of the resonator is affected by the refractive index of both the composite cladding layer and the fiber core. The refractive index of the composite cladding layer (n_{ccl}) increases gradually with the density of TiO_2 NPs with high refractive index on the microfiber surface, leading to the increase of the n_{cav}. The magnetic field distributions $|H_z|$ for the TE modes in the WGM microfibers at different n_{ccl} were simulated by using the finite-element method. With the increase of n_{ccl}, the mode-field intensity distribution of the mode is more restricted to the cladding layer with high refractive index based on the principle of total reflection. The simulated results show the evolution for the TE modes gradually concentrating in the cladding layer with the increase of the n_{ccl}, maintaining stable traveling wave oscillation.

The mode spacing of TE and TM polarizations for WGM laser is determined by several factors, including cavity diameter (D), n_{cav} and ambient refractive index (n_{env}) (supplementary notes in the ESM). According to the simulation showing the positive

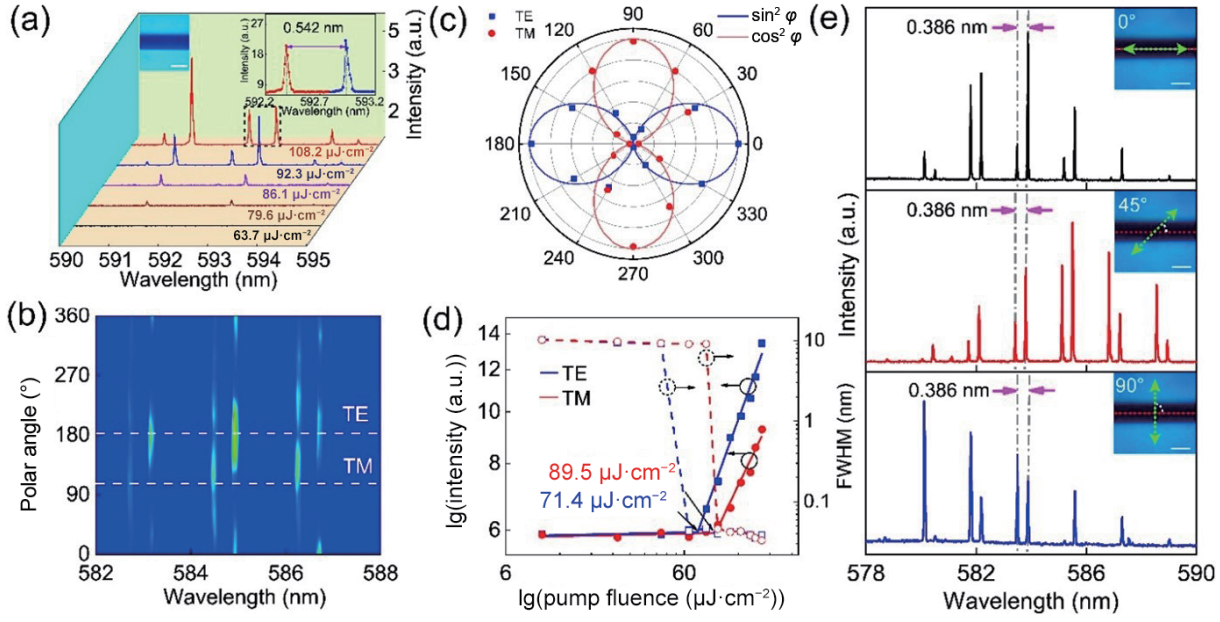

Figure 2 Characterization of lasing properties for the printed microfibers. (a) PL spectra evolution under different pump fluence for the lasing microfiber. The left inset shows corresponding microscopy image of the microfiber with the diameter of 43 μm. Scale bar: 50 μm. The right inset shows a magnified view of two adjacent modes with $\Delta\lambda$ of 0.542 nm. (b) Contour map of angle-dependent polarization of the lasing emissions. (c) Normalized emissions of two sets of lasing modes as a function of detection polarization angle, confirming TE (blue) and TM (red) modes. The solid blue and red lines are curves of $\cos^2\varphi$ and $\sin^2\varphi$, respectively. (d) The dependence of PL intensity and FWHM of TE and TM polarizations on the pump fluence, showing the respective lasing thresholds. (e) The fixed $\Delta\lambda$ of 0.386 nm under different angle between polarization direction of pumping source and axis direction of the microfiber. The right insets show microscopy images of the microfiber for diameter of 46 μm. The red dotted line indicates the axial direction of the microfiber, and green arrows indicate the polarization directions of the pumping source. Scale bar: 50 μm.

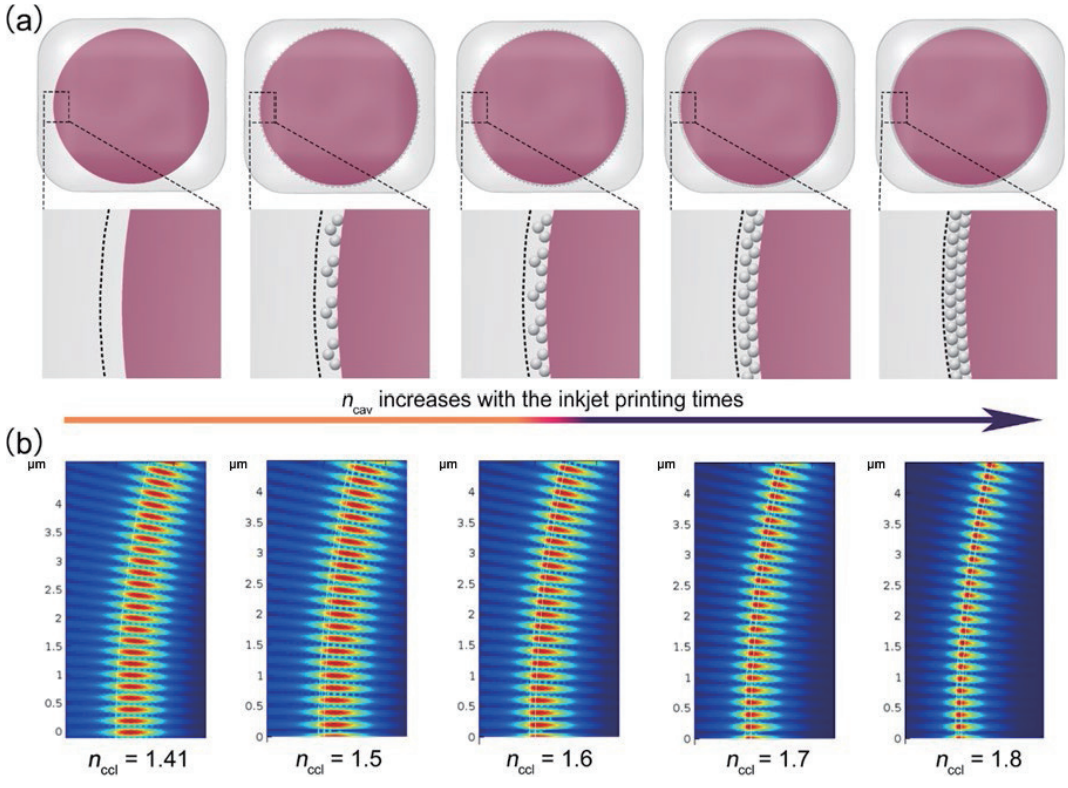

Figure 3 Establishment of the physical models and the mode field distribution of the WGM for the microfiber cavity of the printed microlasers. (a) The schematic physical model of microlasers with different density of TiO_2 nanoparticles to illustrate that n_{cav} increases with the inkjet printing times. The black dotted curves indicate the boundary of the composite cladding layer. (b) Mode field intensity distribution $|H_z|$ of TE modes for the microfibers coated with a composite cladding layer. The refractive index of the composite cladding layer varies from 1.41 to 1.80.

correlation between the NPs density and n_{cav}, we experimentally investigated the effect of the coating TiO_2 NPs on the mode spacing. The microfibers with diameter about 40 μm were coated with TiO_2 NPs via inkjet printing, and the density of the TiO_2 NPs at the targeted spot can be regulated by inkjet printing times (Fig. 4(a)), which can be conducted by designing the printing program. Without TiO_2 NPs on the microfiber, $\Delta\lambda$ is measured to be 0.277 nm. When the microfiber surface is coated with TiO_2 NPs, $\Delta\lambda$ gradually increases from 0.401 to 0.889 nm, as the printing times increase from 1 to 4. Considering the negligible difference of FSR

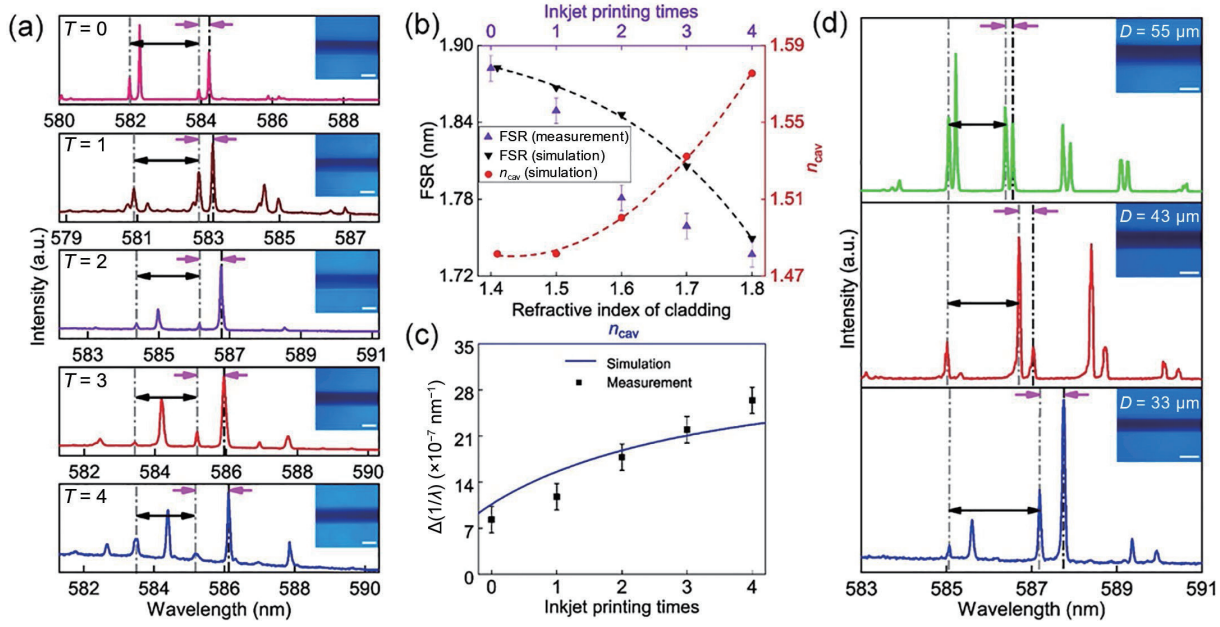

Figure 4 Characterization of lasing mode spacing of TE and TM polarizations for microfibers. (a) The $\Delta\lambda$ increase with inkjet printing times, while the value of FSR decrease with inkjet printing times. With the increase of inkjet times from 0 to 4, the mode spacing between TE and TM polarizations is 0.277, 0.401, 0.606, 0.739 and 0.889 nm, respectively; while the FSR is 1.877, 1.844, 1.776, 1.754 and 1.728 nm, respectively. Insets: corresponding microscopy images of microfibers of 40 μm with different inkjet printing times. Scale bar: 40 μm. (b) The dependence of the simulated FSR and n_{cav} on the n_{ccl}, and the experimental value of FSR (purple triangles) on the inkjet printing times. (c) The dependence of the measured $\Delta 1/\lambda$ on the inkjet printing times, and the simulated value on the n_{cav}. (d) The $\Delta\lambda$ decrease with diameter of the printed microfibers. With the increase of microfiber diameter from 33 to 55 μm, the mode spacing between TE and TM polarizations is 0.569, 0.343 and 0.238 nm, respectively; while the FSR is 2.147, 1.692 and 1.354 nm, respectively. Insets: corresponding microscopy images of microfibers with diameters of 33, 43 and 55 μm. Scale bar: 40 μm.

measured from adjacent TE or TM lasing polarization (Fig. S13 in the ESM), we took the FSR of TM lasing polarization as an example. It is found that the FSR gradually decreases with inkjet printing times. Moreover, the simulated result depicts that the FSR gradually decreases with n_{ccl} (thickness of the composite cladding layer about 80 nm), which increases from 1.41 to 1.80, with the gradual enrichment of the TiO_2 NPs via increasing the inkjet printing times (Fig. 4(b)). Furthermore, n_{cav} gradually increases with the n_{ccl}. As FSR is always estimated from $\lambda^2/\pi D n_{cav}$ for a WGM microresonator, it is reasonable to speculate that the decrease of the FSR is attributed to the variation of n_{cav} via increasing inkjet printing times. This variation of n_{cav} influences the value of FSR, which is consistent with the experiment result. We converted $\Delta\lambda$ to $\Delta 1/\lambda$ to investigate the relationship between the mode spacing and inkjet printing times, and found that $\Delta 1/\lambda$ increases with the inkjet printing times (Fig. 4(c) and Fig. S14 in the ESM), which is fitted well with the simulated results from the Eq. (S4) (supplementary notes in the ESM). These results indicate that the variation of mode spacing between TE and TM polarizations can be attributed to the tunable n_{cav}. Therefore, it can be concluded that $\Delta 1/\lambda$ can be regulated effectively by modulating n_{cav} through printing a layer of high refractive index dielectric material TiO_2 NPs, and we expect that other high refractive index dielectric material can also play a similar role in the modulation.

In addition, we compared the mode spacing of TE and TM polarizations for the printed microfibers with different diameters, and found that $\Delta\lambda$ (or $\Delta 1/\lambda$) decreased with the diameter, as well with the FSR (Fig. 4(d)). The experiment data is fitted with a linear slope (πn_{cav}) about 4.69 (Fig. S15 in the ESM), showing that FSR is inversely proportional to the microfiber diameter, verifying the WGM-type cavity resonances. The n_{cav} is calculated to be 1.49, in good agreement with the obtained refractive index of the mixed PVA-SDS-RhB film as 1.5 measured by an ellipsometer. Besides, the Q exhibits a nearly positive correlation with microfiber diameters in the range from 35 to 88 μm. (Fig. S16 in the ESM). The calculated angular mode number of TE and TM polarizations is closely consistent with the experimental results, as shown in Fig. S17 in the ESM.

Benefiting from PDMS encapsulation, the printed microlaser arrays can be made into a free-standing membrane, and the printed lasing microfiber can operate stably under a nanosecond lasing pumping over a long time and exhibits stable mode spacing of TE and TM polarizations (Fig. 5(a) and Fig. S18 in the ESM). Though redshift of the wavelength of TE and TM modes is observed under the nanosecond laser pumping mainly due to the thermo-optical effect [52], the mode spacing is generally stable. Besides, no difference can be distinguished under natural or UV light before and after printing TiO_2 NPs with small nanoscale sizes on microfibers (Fig. S19 in the ESM). By depositing several droplets *in-situ* via multiple precise positioning of the ink by a digital program, TiO_2 NPs density on surface of the microfibers can be region-selectively tuned to achieve the patterning of microlasers with different n_{cav}. Based on these, mode spacing between TE and TM lasing polarizations can be regulated at arbitrary position, which can be applied in the information encryption. It should be noted that $\Delta 1/\lambda$ is also influenced by the microfiber diameter (Fig. 5(b)). This diameter nonuniformity in the polymer microfibers resulted from the fabrication process can lead to false information. Therefore, we elaborately extracted $\Delta(1/\lambda)/\mathrm{FSR}$ as the coding element to store information to exclude the uneven size effect of the resonant cavity in the lasing device (supplementary notes in the ESM). It is found that $\Delta(1/\lambda)/\mathrm{FSR}$ varies from 4.4×10^{-7} to 15.3×10^{-7} nm^{-2} when the inkjet printing times range from 0 to 4 (Fig. 5(c) and Fig. S20 in the ESM). The relationship between the specific spectral information of polarization modes and n_{cav} provides a strategy for information recording, which can convert messages into a set of spectral signals. As a proof of concept, we can divide the region of a lasing microfiber into m cells, and different distribution density of TiO_2 NPs can be regulated on each cell to encode it by a designable printing digital program. With this coding strategy, we can write $5^{m\times n}$ information in a lasing membrane composed of n

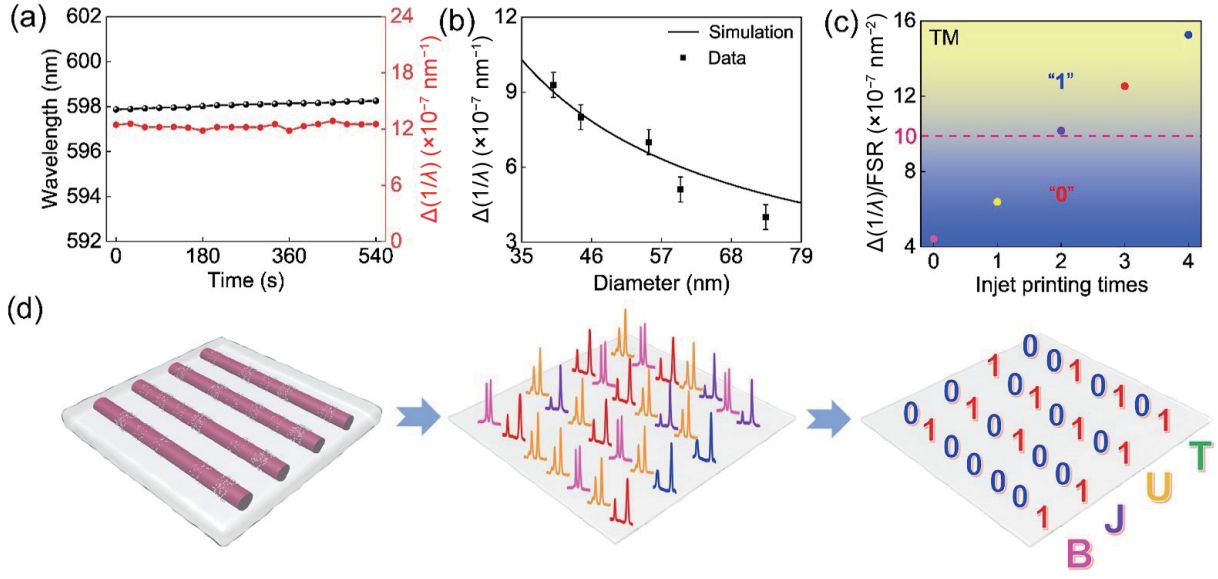

Figure 5 Demonstration of the free-standing WGM lasing microfiber arrays membrane and its application in information encryption. (a) Lasing modes of TM polarizations and the corresponding $\Delta 1/\lambda$ under continuous pumping for 9 min, showing the stable of this strategy. (b) The dependence of measured and simulated value of $\Delta 1/\lambda$ on microfiber diameter. (c) The dependence of $\Delta(1/\lambda)/\mathrm{FSR}$ for TM lasing polarizations on inkjet printing times. The red dotted line represents the threshold value of 10.0×10^{-7} nm^{-2}. (d) The decryption process of the printed microlaser arrays membrane. The lasing spectra is converted into ASCII codes, and the hiding information of "BJUT" can be read out.

microfibers in the array. For instance, the spectral encoding sequences are used to encrypt the message of "BJUT", which is translated into a digital program that is used to inkjet print TiO_2 NPs inks on the surface of the lasing microfiber arrays. The coding rule can be also adjusted to further improve the security level of encryption. Applying a binary coding, we took 10.0×10^{-7} nm^{-2} as the threshold value, when $\Delta(1/\lambda)/\mathrm{FSR}$ is smaller or larger than the above value, the coding element is defined as "0" or "1". Furthermore, the permutation and combination of these coding elements can be determined by the printing program and the selected threshold value. For the decryption process as shown in Fig. 5(d), the emissive spectra of the WGM laser pattern on the encrypted microlaser arrays are measured to obtain the value of $\Delta(1/\lambda)/\mathrm{FSR}$ at each pixel, which can be converted into a series of ASCII codes. If the right receiver obtains the encryption rules, they can read out the right information "BJUT". The covert data recording process can be completed via inkjet printing TiO_2 ink on the microlaser arrays simply by a digital programmable printer (Fig. S21 in the ESM), and can be read out by measuring the lasing signals of the printed lasing microfibers. Through encoding each pixel with different information modulated by the distribution density of TiO_2 NPs deposits, data encoding with different information can be achieved, and can be customized according to the user's need. It should be noted that the value of $\Delta(1/\lambda)/\mathrm{FSR}$ varies under different bending conditions of the membrane (Fig. S22 in the ESM), which can increase the decryption complexity to some degree. Nevertheless, excessive bending situation should be avoided to maintain the restorability of the resonant cavity. Given that the microlaser arrays are large-area processable (Fig. S23 in the ESM), we can encode different regions with predesigned information to achieve large-capacity optical encryption. Although the two-dimensional macroscale encrypted chip containing thousands of discrete microlasers that can be written in diverse covert information, the encoding process through printing is completed within a few minutes using a single-nozzle printing machine.

4 Conclusions

In this work, we demonstrate a facile and versatile strategy to fabricate a free-standing microlaser arrays with tunable polarization modes, and show the application in information encryption. By region selectively modulating the refractive index of the resonant cavity through inkjet printing high-refractive-index NPs on the microfiber lasers, large-area processable microlaser arrays with programmable mode spacing of TE and TM polarizations are achieved. It is found that the coating of TiO_2 NPs with different density can effectively tune the effective refractive index of the microcavity, and the interface scattering can be reduced to maintain regular lasing modes by the encapsulation into transparent PDMS medium. Furthermore, we extract the ratio of wavenumber spacing to FSR of the microlaser to eliminate the interruption from uneven size produced in the polymer microfibers, and encode the microlaser arrays with arbitrary encryption information. It is the first time to report the information encryption based on the polymer microfiber lasers platform. The fabrication of the microfibers and the encoding approach by inkjet printing are both facile, low-cost and large area processable, showing promise in the development of printable flexible photonic device.

Acknowledgement

The authors would like to acknowledge the National Natural Science Foundation of China (NSFC) (Nos. 52203252 and 61822501) and the Beijing Natural Science Foundation (No. Z180015) for financial support.

Electronic Supplementary Material: Supplementary material (additional calculation formulas, simulations, characterization, schematic of the encryption process and fluorescence photographs) is available in the online version of this article at https://doi.org/10.1007/s12274-023-5709-8.

References

[1] Gu, M.; Li, X. P.; Cao, Y. Y. Optical storage arrays: A perspective for future big data storage. *Light Sci. Appl.* **2017**, *3*, e177.

[2] Hu, Z. Y.; Comeras, J. M. M. L.; Park, H.; Tang, J. S.; Afzali, A.; Tulevski, G. S.; Hannon, J. B.; Liehr, M.; Han, S. J. Physically unclonable cryptographic primitives using self-assembled carbon

nanotubes. *Nat. Nanotechnol.* **2016**, *11*, 559–565.
[3] Lee, J.; Bisso, P. W.; Srinivas, R. L.; Kim, J. J.; Swiston, A. J.; Doyle, P. S. Universal process-inert encoding architecture for polymer microparticles. *Nat. Mater.* **2014**, *13*, 524–529.
[4] Deng, J.; Li, Z. L.; Li, J. X.; Zhou, Z.; Gao, F.; Qiu, C. H.; Yan, B. Metasurface-assisted optical encryption carrying camouflaged information. *Adv. Optical Mater.* **2022**, *10*, 2200949.
[5] Qu, G. Y.; Yang, W. H.; Song, Q. H.; Liu, Y. L.; Qiu, C. W.; Han, J. C.; Tsai, D. P.; Xiao, S. M. Reprogrammable meta-hologram for optical encryption. *Nat. Commun.* **2020**, *11*, 5484.
[6] Yang, Q. S.; Xie, Z. J.; Zhang, M. R.; Ouyang, X.; Xu, Y.; Cao, Y. Y.; Wang, S. C.; Zhu, L. W.; Li, X. P. Ultra-secure optical encryption based on tightly focused perfect optical vortex beams. *Nanophotonics* **2022**, *11*, 1063–1070.
[7] Huang, F. T.; Weng, Y. H.; Lin, Y. X.; Zhang, X. C.; Wang, Y. F.; Chen, S. G. Wetting-enhanced structural color for convenient and reversible encryption of optical information. *ACS Appl. Mater. Interfaces* **2021**, *13*, 42276–42286.
[8] Li, K. X.; Li, H. Z.; Guo, D.; Zhan, X. Q.; Li, A.; Cai, Z. R.; Li, Z.; Qu, Z. Y.; Xue, L. L.; Li, M. Z. et al. 3D optical heterostructure patterning by spatially allocating nanoblocks on a printed matrix. *ACS Nano* **2022**, *16*, 14838–14848.
[9] Gong, X. R.; Qiao, Z.; Liao, Y. K.; Zhu, S.; Shi, L.; Kim, M.; Chen, Y. C. Enzyme-programmable microgel lasers for information encoding and anti-counterfeiting. *Adv. Mater.* **2022**, *34*, 2107809.
[10] Tan, M. L.; Li, F.; Wang, X.; Fan, R. W.; Chen, G. Y. Temporal multilevel luminescence anticounterfeiting through scattering media. *ACS Nano* **2020**, *14*, 6532–6538.
[11] Luo, T.; Zhou, T.; Qu, J. L. Lifetime division multiplexing by multilevel encryption algorithm. *ACS Nano* **2021**, *15*, 6257–6265.
[12] Gu, L.; Wu, H. W.; Ma, H. L.; Ye, W. P.; Jia, W. Y.; Wang, H.; Chen, H. Z.; Zhang, N.; Wang, D. D.; Qian, C. et al. Color-tunable ultralong organic room temperature phosphorescence from a multicomponent copolymer. *Nat. Commun.* **2020**, *11*, 944.
[13] Xie, Y.; Song, Y. P.; Sun, G. T.; Hu, P. F.; Bednarkiewicz, A.; Sun, L. N. Lanthanide-doped heterostructured nanocomposites toward advanced optical anti-counterfeiting and information storage. *Light Sci. Appl.* **2022**, *11*, 150.
[14] Zhou, Q. W.; Qiu, X. C.; Su, X. L.; Liu, Q.; Wen, Y.; Xu, M.; Li, F. Y. Light-responsive luminescent materials for information encryption against burst force attack. *Small* **2021**, *17*, 2100377.
[15] Zhou, Y. S.; Zhao, G.; Bian, J. M.; Tian, X. L.; Cheng, X. J.; Wang, H.; Chen, H. Y. Multiplexed SERS barcodes for anti-counterfeiting. *ACS Appl. Mater. Interfaces* **2020**, *12*, 28532–28538.
[16] Li, D. Y.; Tang, L. H.; Wang, J. J.; Liu, X. J.; Ying, Y. B. Multidimensional SERS barcodes on flexible patterned plasmonic metafilm for anticounterfeiting applications. *Adv. Optical Mater.* **2016**, *4*, 1475–1480.
[17] Feng, J. G.; Wen, W.; Wei, X.; Jiang, X. Y.; Cao, M. Y.; Wang, X. D.; Zhang, X. Q.; Jiang, L.; Wu, Y. C. Random organic nanolaser arrays for cryptographic primitives. *Adv. Mater.* **2019**, *31*, 1807880.
[18] Chen, X. L.; Wang, K. Y.; Shi, B. R.; Liu, T. H.; Chen, R. M.; Zhang, M. Y.; Wen, W. J.; Xing, G. C.; Wu, J. B. All-inorganic perovskite nanorod arrays with spatially randomly distributed lasing modes for all-photonic cryptographic primitives. *ACS Appl. Mater. Interfaces* **2021**, *13*, 30891–30901.
[19] Hill, M. T.; Gather, M. C. Advances in small lasers. *Nat. Photon.* **2014**, *8*, 908–918.
[20] Liu, H.; Yu, H. R.; Dai, L.; Li, Z.; Chen, J. J. Low-threshold and narrow-linewidth perovskite microlasers pumped by a localized waveguide source. *Nanophotonics* **2021**, *10*, 3477–3485.
[21] Ge, L.; Cao, H.; Stone, A. D. Condensation of thresholds in multimode microlasers. *Phys. Rev. A* **2017**, *95*, 023842.
[22] Jiang, L. D.; Shi, L. L.; Huang, D. M.; Luo, J.; Gao, Q. R.; Lan, T. Y.; Bai, M. X.; Li, J. L.; Dang, L. Y.; Huang, L. G. et al. Control of polarization switching in a VCSEL via resonant feedback from a whispering-gallery-mode cavity. *Opt. Lett.* **2022**, *47*, 862–865.
[23] Chen, F.; Xu, C. X.; Xu, Q. Y.; Zhu, Z.; Qin, F. F.; Manohari, A. G.; Zhu, Y. Z. Lasing mode evolution and regulation of the perovskite $CH_3NH_3PbBr_3$. *J. Mater. Chem. C,* **2017**, *5*, 9238–9241.
[24] Rashidi, M.; Haggren, T.; Su, Z. C.; Jagadish, C.; Mokkapati, S.; Tan, H. H. Managing resonant and nonresonant lasing modes in GaAs nanowire random lasers. *Nano Lett.* **2021**, *21*, 3901–3907.
[25] Zhu, H. M.; Fu, Y. P.; Meng, F.; Wu, X. X.; Gong, Z. Z.; Ding, Q.; Gustafsson, M. V.; Trinh, M. T.; Jin, S.; Zhu, X. Y. Lead halide perovskite nanowire lasers with low lasing thresholds and high quality factors. *Nat. Mater.* **2015**, *14*, 636–642.
[26] Triandaf, I.; Schwartz, I. B. Quality Factor Control in a lasing microcavity model. *Phys. Rev. E* **2000**, *61*, 3601–3609.
[27] Jin, L. M.; Chen, X.; Wu, Y. K.; Ai, X. Z.; Yang, X. L.; Xiao, S. M.; Song, Q. H. Dual-wavelength switchable single-mode lasing from a lanthanide-doped resonator. *Nat. Commun.* **2022**, *13*, 1727.
[28] Zhang, H. H.; Liao, Q.; Wu, Y. S.; Zhang, Z. Y.; Gao, Q. G.; Liu, P.; Li, M. L.; Yao, J. N.; Fu, H. B. 2D Ruddlesden-Popper perovskites microring laser array. *Adv. Mater.* **2018**, *30*, 1706186.
[29] Shi, Z. F.; Zhang, F.; Yan, J. J.; Zhang, Y.; Chen, X.; Chen, S.; Wu, D.; Li, X. J.; Zhang, Y.; Shan, C. X. Robust frequency-upconversion lasing operated at 400 K from inorganic perovskites microcavity. *Nano Res.* **2022**, *15*, 492–501.
[30] Zhang, Q.; Ha, S. T.; Liu, X. F.; Sum, T. C.; Xiong, Q. H. Room-temperature near-infrared high-Q perovskite whispering-gallery planar nanolasers. *Nano Lett.* **2014**, *14*, 5995–6001.
[31] Zhang, L.; Zhang, J. S.; Shang, Q. Y.; Song, J. P.; Li, C.; Du, W. N.; Chen, S. L.; Liu, X. F.; Zou, B. S.; Gao, P. et al. Ultrafast antisolvent growth of single-crystalline $CsPbCl_3$ microcavity for low-threshold room temperature blue lasing. *ACS Appl. Mater. Interfaces* **2022**, *14*, 21356–21362.
[32] Lin, G. P.; Coillet, A.; Chembo, Y. K. Nonlinear photonics with high-*Q* whispering-gallery-mode resonators. *Adv. Opt. Photon.* **2017**, *9*, 828–890.
[33] Wei, G. Q.; Wang, X. D.; Liao, L. S. Recent advances in organic whispering-gallery mode lasers. *Laser Photon. Rev.* **2020**, *14*, 2000257.
[34] Hu, B. L.; Zhang, Z. W.; Zhang, H. X.; Zheng, L. Y.; Xiong, W.; Yue, Z. C.; Wang, X. Y.; Xu, J. Y.; Cheng, Y.; Liu, X. J. et al. Non-Hermitian topological whispering gallery. *Nature* **2021**, *597*, 655–659.
[35] Yang, S. C.; Wang, Y.; Sun, H. D. Advances and prospects for whispering gallery mode microcavities. *Adv. Opt. Mater.* **2015**, *3*, 1136–1162.
[36] Lam, C. C.; Leung, P. T.; Young, K. Explicit asymptotic formulas for the positions, widths, and strengths of resonances in mie scattering. *J. Opt. Soc. Am. B* **1992**, *9*, 1585–1592.
[37] Vollmer, F.; Arnold, S. Whispering-gallery-mode biosensing: Label-free detection down to single molecules. *Nat. Methods* **2008**, *5*, 591–596.
[38] Yu, X. C.; Tang, S. J.; Liu, W. J.; Xu, Y. L.; Gong, Q. H.; Chen, Y. L.; Xiao, Y. F. Single-molecule optofluidic microsensor with interface whispering gallery modes. *Proc. Natl. Acad. Sci. USA* **2022**, *119*, e2108678119.
[39] Shao, L. B.; Jiang, X. F.; Yu, X. C.; Li, B. B.; Clements, W. R.; Vollmer, F.; Wang, W.; Xiao, Y. F.; Gong, Q. H. Detection of single nanoparticles and lentiviruses using microcavity resonance broadening. *Adv. Mater.* **2013**, *25*, 5616–5620.
[40] Noto, M.; Keng, D.; Teraoka, I.; Arnold, S. Detection of protein orientation on the silica microsphere surface using transverse electric/transverse magnetic whispering gallery modes. *Biophys. J.* **2007**, *92*, 4466–4472.
[41] Foreman, M. R.; Swaim, J. D.; Vollmer, F. Whispering gallery mode sensors. *Adv. Opt. Photon.* **2015**, *7*, 168–240.
[42] Ge, K.; Guo, D.; Niu, B.; Xu, Z. Y.; Ruan, J.; Zhai, T. R. Pump-controlled RGB single-mode polymer lasers based on a hybrid 2d-3d μ-cavity for temperature sensing. *Nanophotonics* **2021**, *10*, 4591–4599.
[43] Fan, Y. Q.; Zhang, C. H.; Gao, Z. H.; Zhou, W.; Hou, Y.; Zhou, Z. H.; Yao, J. N.; Zhao, Y. S. Randomly induced phase transformation in silk protein-based microlaser arrays for anticounterfeiting. *Adv. Mater.* **2021**, *33*, 2102586.
[44] Wang, K.; Liang, J.; Chen, R.; Gao, Z. H.; Zhang, C.; Yan, Y. L.; Yao, J. N.; Zhao, Y. S. Geometry-programmable perovskite microlaser patterns for two-dimensional optical encryption. *Nano Lett.* **2021**, *21*, 6792–6799.

[45] Gao, Z. H.; Wang, K.; Yan, Y. L.; Yao, J. N.; Zhao, Y. S. Smart responsive organic microlasers with multiple emission states for high-security optical encryption. *Nat. Sci. Rev.* **2021**, *8*, nwaa162.
[46] Yang, S. C.; Eugene, T. Y. K.; Wang, Y.; Zhao, X.; Demir, H. V.; Sun, H. D. Wavelength tuning of the spirally drawn whispering gallery mode microfiber lasers and the perspectives for sensing applications. *Opt. Express* **2017**, *25*, 2618–2626.
[47] Ta, V. D.; Chen, R.; Ma, L.; Ying, Y. J.; Sun, H. D. Whispering gallery mode microlasers and refractive index sensing based on single polymer fiber. *Laser Photon. Rev.* **2013**, *7*, 133–139.
[48] Ruan, J.; Guo, D.; Niu, B.; Ge, K.; Zhai, T. R. Whispering-gallery-mode full-color laser textiles and their anticounterfeiting applications. *NPG Asia Mater.* **2022**, *14*, 62.
[49] Li, B. B.; Wang, Q. Y.; Xiao, Y. F.; Jiang, X. F.; Li, Y.; Xiao, L. X.; Gong, Q. H. On chip, high-sensitivity thermal sensor based on high-*Q* polydimethylsiloxane-coated microresonator. *Appl. Phys. Lett.* **2010**, *96*, 251109.
[50] Wang, X. D.; Liao, Q.; Li, H.; Bai, S. M.; Wu, Y. S.; Lu, X. M.; Hu, H. Y.; Shi, Q.; Fu, H. B. Near-infrared lasing from small-molecule organic hemispheres. *J. Am. Chem. Soc.* **2015**, *137*, 9289–9295.
[51] Zhang, Y. X.; Pu, X. Y.; Feng, L.; Han, D. Y.; Ren, Y. T. Polarization characteristics of whispering-gallery-mode fiber lasers based on evanescent-wave-coupled gain. *Opt. Express* **2013**, *21*, 12617–12628.
[52] Yang, X. F.; Lyu, Z. Y.; Dong, H.; Sun, L. D.; Yan, C. H. Lanthanide upconverted microlasing: Microlasing spanning full visible spectrum to near-infrared under low power, CW pumping. *Small* **2021**, *17*, 2103140.